buildings

MDPI

Article

Mechanical Activation of Portland Cement Improves Resistance to Acid Attack: Insights from 4D X-Ray Computed Tomography

Elena Semenova [1], Farid Shakirzyanov [1], Ruslan Ibragimov [2], Rail Kadyrov [1], Tatyana Baltina [1], Bulat Tazyukov [1], Oleg Gerasimov [1] and Oskar Sachenkov [1,*]

[1] N.I. Lobachevsky Institute of Mathematics and Mechanics, Kazan Federal University, Kazan 420008, Russia; elena.semionova2011@gmail.com (E.S.); faritbox@mail.ru (F.S.); rail7777@gmail.com (R.K.); tvbaltina@gmail.com (T.B.); bulat.tazioukov@kpfu.ru (B.T.); olevgerasimov@kpfu.ru (O.G.)

[2] Institute of Civil Engineering, Kazan State University of Architecture and Engineering, Kazan 420043, Russia; rusmag007@yandex.ru

* Correspondence: 4works@bk.ru

Abstract

Concrete structures exposed to biological attack undergo degradation caused by organic acids produced by microorganisms. To improve the resistance of cementitious materials, this study applied mechanical activation of Portland cement using a vortex layer device. Porosity and compressive strength of control and mechanically activated hardened cement paste (HCP) specimens were evaluated after 0, 14, and 28 days of exposure to a model acidic environment (pH 3, a mixture of carboxylic acids). Spatiotemporal heterogeneity of degradation in control and activated HCP was assessed for the first time by 4D X-ray computed tomography, which tracked individual pores across the same time points and revealed degradation patterns inaccessible to bulk measurements. Mechanical activation was found to increase the initial compressive strength by 33% (59.3 MPa vs. 44.5 MPa). After 28 days, the activated specimens retained 75% of their initial strength, compared with 62% for the control ones. Despite higher initial porosity (1.5% vs. 1%), the mechanically activated specimens exhibited lower volumetric loss (27% vs. 56%) and maintained spatial stability of the pore framework. These findings support the potential of this approach for structures operating under microbiological corrosion conditions.

Keywords: X-ray computed tomography; concrete degradation; aggressive environment; porosity; mechanical activation; hardened cement paste

Check for updates

Academic Editor: Salvatore Verre

Received: 2 September 2026
Revised: 9 October 2026
Accepted: 11 October 2026
Published: 14 October 2026

Copyright: © 2026 by the authors. Licensee MDPI, Basel, Switzerland. This article is an open access article distributed under the terms and conditions of the Creative Commons Attribution (CC BY) license.

1. Introduction

Concrete structures in service are exposed to various aggressive environmental factors, including temperature fluctuations, moisture, chemical agents, and biological agents [1,2]. Among these, the least studied but critically important is the effect of microbial metabolic products, leading to biodeterioration of materials. Such processes are particularly intense in industrial areas of chemical, medical, and food industries, as well as in sewer systems and wastewater treatment facilities [3,4]. Microbial metabolism produces organic and inorganic acids, alkalis, peroxides, and hydrogen sulfide. These compounds lower the pH of the environment and dissolve the hydration products of HCP, primarily portlandite ($Ca(OH)_2$) and calcium silicate hydrates (C-S-H gels) [5]. This leads to decalcification, increased porosity, reduced strength, and accelerated further degradation of structures [6–9]. However, this process is not limited to porosity increase alone. Simultaneously, mechanisms of local pore infilling operate, temporarily slowing acid penetration into the material. This

effect is caused both by precipitation of secondary reaction products in pores and by exposure of clinker grains, which form a mechanical barrier that modifies the diffusivity of the degraded layer [10–13].

The activity of biocorrosion is largely determined by the pore structure characteristics of the material, which control the penetration rate of aggressive agents. For example, in [14], the effect of microencapsulated phase change materials on the pore structure and gas permeability of geopolymers was studied. One effective way to improve concrete resistance to acid attack is mechanical activation of Portland cement in a vortex layer device. This process significantly increases the specific surface area of the binder, modifies the pore structure, and improves the performance of composite materials [15–17]. In a previous study [18] on the same HCP specimens, a physical–numerical model of degradation in a model acid medium was developed, and data on the kinetics of mass change and compressive strength were obtained. The present work extends those results by applying 4D X-ray computed tomography with individual pore tracking, which allowed quantitative assessment of spatiotemporal heterogeneity of degradation.

Traditional degradation assessment methods (mechanical tests, mass change, and water absorption measurements) provide only integral characteristics, without detailed analysis of the spatiotemporal evolution of internal structure. An integrated approach combining mechanical tests with pore structure analysis is also being developed in studies on sustainable cementitious materials, for example [19]. A promising non-destructive method for quantitative analysis of pore space with high spatial resolution is X-ray computed tomography (XCT) [20–23]. In recent years, 4D approaches have gained particular value, allowing tracking of individual pores and microstructure evolution over time on the same specimen. Such tracking provides insight into spatiotemporal heterogeneity of degradation processes, which is fundamentally inaccessible to traditional methods [24,25].

XCT has already been used to study the degradation of cementitious materials; however, in most cases the analysis remained integral or concerned other processes. In [26], micro-CT was used to study the destruction of hardened cement paste under acid attack: the method made it possible to record changes in the microstructure and the formation of a degraded layer, but only general changes in porosity and damage depth were assessed, without tracking individual pores over time. In a previous study [27], 4D micro-CT was used to analyze the evolution of the pore network of slag cement pastes during hardening, but specific pores were not tracked. In [28], 4D XCT was used to quantitatively characterize pore evolution after high-temperature exposure, while in [24] it was used to study reinforcement corrosion, where cracks, voids, and corrosion products were tracked, but not individual pores. Thus, 4D XCT has already been used, but mainly for hydration, thermal exposure, and reinforcement corrosion, whereas individual pore tracking under biocorrosion has not previously been performed.

In [29], it was confirmed that activation in a vortex layer device significantly increases the specific surface area of cement; however, the combination of mechanical activation with 4D XCT to study degradation under biocorrosion conditions has not been previously investigated. Regarding concrete biocorrosion, there are known studies in which XCT was used to visualize bacterial weathering of concrete and stone. In particular, in [30], micro-CT was used to monitor the biological weathering of building materials and to study the effect of organic acids—products of microbial metabolism—on concrete and stone using micro-CT. However, these studies did not include a 4D approach with tracking of individual pores and did not consider mechanically activated cement. Consequently, although XCT and 4D XCT have already been used to study the degradation of cementitious materials, their combination with mechanically activated Portland cement and a biocorrosion model, as well as individual pore tracking over time, has not been performed previously.

Despite research on cement activation and separately on 4D-XCT of concrete degradation, their combination to study pore structure evolution under organic biocorrosion conditions has not been previously performed. This work aimed to experimentally evaluate how a model acid medium simulating microbial metabolic products affects porosity and strength in HCP based on control and mechanically activated Portland cement. A further aim was to assess pore space dynamics through individual pore tracking. For the first time, 4D-XCT with individual pore tracking over time was used to quantitatively estimate the spatiotemporal heterogeneity of degradation. It was found that despite higher initial porosity, mechanically activated specimens exhibited two-fold lower volumetric loss and maintained spatial stability of the pore framework, confirming the promise of this approach for structures operating under microbiological corrosion conditions.

2. Materials and Methods

2.1. Specimens

Two types of specimens were prepared: control specimens, made with untreated Portland cement, and activated specimens, made with mechanically activated Portland cement. Portland cement CEM I 42.5 R (Novotroitsk, Russia) complying with EN 197-1 was used to produce HCP [31]. According to the manufacturer's data sheet, its mineralogical composition was as follows: C_3S (alite) 64–65%, C_2S (belite) 11–13%, C_3A (tricalcium aluminate) 5–6%, and C_4AF (tetracalcium aluminoferrite) 14–15%, with MgO and SO_3 content not exceeding 1%. For the activated specimens, this Portland cement was additionally mechanically activated in a vortex layer device model 297 (Regionmettrans, Nizhny Novgorod, Russia). Ferromagnetic elements within the device are set in motion by a rotating electromagnetic field, producing simultaneous particle-size reduction and mechanical activation of the cement. Treatment was applied cyclically, for 5 min per batch of 1 kg, at an electromagnetic field frequency of 70 Hz and a ferromagnetic-media-to-material mass ratio of 0.4. The unactivated Portland cement had a specific surface area of 315 m^2/kg, which increased to 580 m^2/kg after mechanical activation, as determined by the Blaine method. Specific surface area was also determined by the BET method using a Quantachrome Nova 1200e surface area and pore size analyzer. Mechanical activation increased the BET specific surface area from 865 m^2/kg to 2075 m^2/kg, with a nonlinear change in particle surface area during treatment.

HCP was prepared by mixing Portland cement with water to normal consistency according to EN 196-3 [32]. Normal consistency was determined separately for the control and activated cement, yielding the same water-to-cement ratio of 0.27 for both. The mixture was cast into metal molds with dimensions of 20 × 20 × 20 mm. ASTM C109/C109M [33], EN 196-1 [34], and ISO 679:2009 [35] standards specify specimens of 50 × 50 × 50 mm or 40 × 40 × 160 mm. However, due to the specific requirements of 4D XCT, we were forced to use research specimens of 20 × 20 × 20 mm. The specimens were cured under natural curing conditions at 20 ± 2 °C and 80 ± 5% relative humidity for 28 days.

2.2. Medium

A mixture of carboxylic acids typical of fungal and bacterial metabolism was used as a model medium simulating microbial metabolic products: acetic acid 1980 mg/L, citric acid 16,020 mg/L, and malic acid 400 mg/L [36–38]. To accelerate the tests, the component concentrations were set at a level providing intense but controlled degradation of the material. The specimens were immersed in 3 L of the model medium, with the upper face of each specimen positioned approximately 4 cm below the solution surface, giving a specimen-to-medium volume ratio of 0.09 (mm^3/mm^3). The temperature was maintained at 20 ± 1 °C. The pH was adjusted to 3 and monitored using a 150 MI pH meter (Moscow,

Russia). Fresh medium was added as needed to maintain this value. The medium was stirred every 24 h of exposure. The exposure setup is shown in Figure 1.

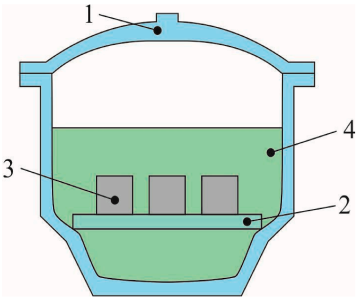


Figure 1. Schematic of the test setup in the model medium: 1—desiccator; 2—mesh support for specimens; 3—tested specimens; 4—model medium.

2.3. Experimental Design

Nine specimens of each type (control and mechanically activated) were prepared for the study. The experiment was divided into three main stages of material assessment: before exposure to the aggressive medium (0 days), and after 14 and 28 days of exposure. One specimen was selected for XCT scanning and was scanned at all test stages. After each scan, this specimen was returned to the model medium for continued exposure, providing longitudinal tracking of the evolution of its pore structure. Three specimens from each group were used for mechanical testing and were destroyed during the experiment. At the 28-day stage, the specimen previously used for XCT scanning was included in the batch of three specimens subjected to compressive testing and was thus also destroyed at this final stage. The measurement scheme was the same for both groups and is presented in Figure 2.

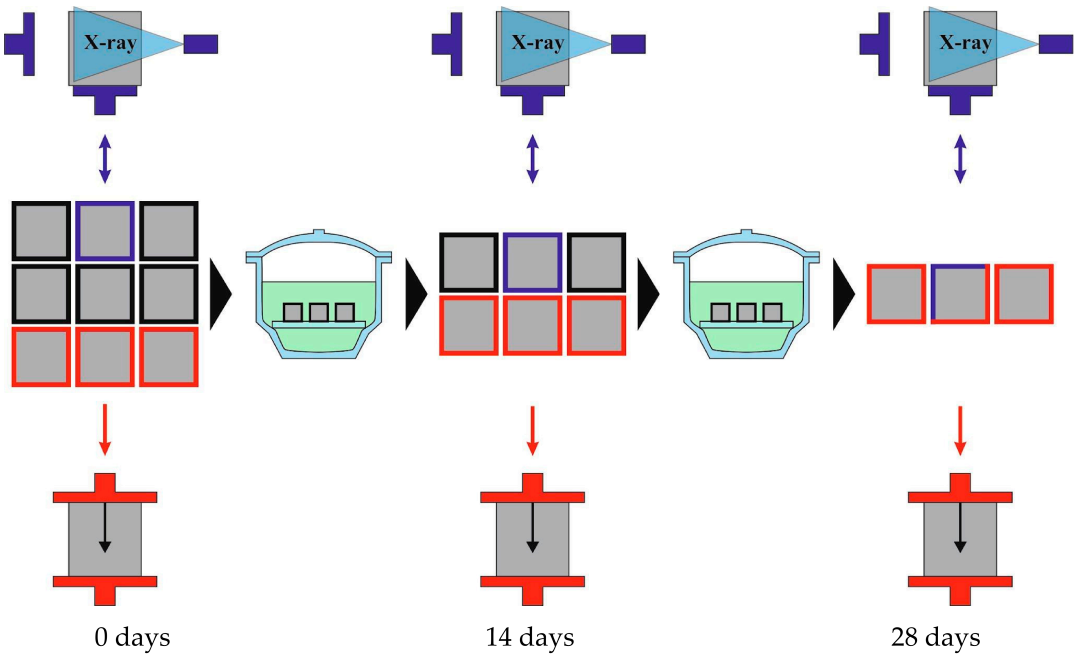


Figure 2. Experiment design.

2.4. Mechanical Testing

Compressive strength was determined on a series of three specimens. The tests were performed using an electromechanical universal testing machine IR 5082-5 (Ivanovo,

Russia) at a loading rate of 0.6 MPa/s according to EN 12390-3 [39]. The reported result is the average value from three measurements.

2.5. XCT Scanning

Before each scan, the specimen was removed from the desiccator and allowed to surface-dry under ambient laboratory conditions for 2 h. Scanning was performed using a micro-nano-focus system Phoenix V | tome | X S240 (Waygate Technologies, Wunstorf, Germany) at the XCT laboratory of the Institute of Geology and Petroleum Technologies, Kazan (Volga Region) Federal University. The system is equipped with two X-ray tubes: a micro-focus tube with a maximum accelerating voltage of 240 kV and power of 320 W, and a nano-focus tube with a maximum accelerating voltage of 180 kV and power of 15 W. Volume reconstruction was carried out using datos | x reconstruction software (Waygate Technologies, Germany).

Scans were acquired using the micro-focus tube at a voltage of 160 kV and a current of 180 μA, with a 0.5 mm copper filter to reduce beam hardening. Each scan comprised 1200 projections, with an exposure time of 200 ms per projection averaged over 3 frames. The voxel size during scanning was 32.432 × 32.432 × 32.432 μm. The scanned field of view measured approximately 2.5 × 2.5 × 2.5 cm, larger than the 2 cm specimen to keep its edges fully within the reconstructed volume and avoid truncation. The resulting arrays varied slightly in size due to manual adjustment, with a linear dimension of approximately 750 voxels.

2.6. Segmentation and Specimen-Scale Quantification

Thus, the input data for subsequent processing is a three-dimensional array whose elements represent the X-ray density of the volume element (1), where the index l denotes the scanning time point (0, 14, 28) and m denotes the specimen type (control or activated). This allows physical interpretation of the quantitative values. The raw data were segmented using a multilevel Otsu method, a histogram-based approach that extends the classical two-class algorithm [40,41]. Instead of a single threshold, the histogram is partitioned into several classes by maximizing between-class variance. In this study, three classes were used, corresponding to air, cement, and holder. In the subsequent analysis, the air and cement segments (2) were processed. For this purpose, the pore space was defined, i.e., all simply connected, closed, non-overlapping subsets corresponding to air were identified (3). Both fractions are shown in Figure 3.

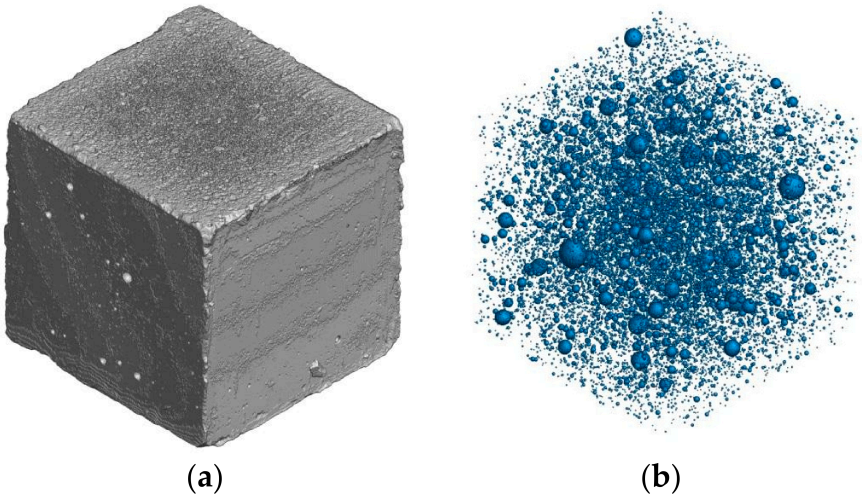


Figure 3. Segmented CT data: (**a**) matrix, (**b**) pore space.

The total specimen volume was calculated as the number of voxels belonging to the matrix and pore-space fractions combined, multiplied by the voxel volume; porosity was then defined as the ratio of the pore-space volume to this total specimen volume.

$$CT^{lm} = \left\{ CT_{ijk}^{lm} \right\},\ CT_{ijk}^{lm} \in R,\ ijk \in \{I, J, K\} \tag{1}$$

$$CT^{lm} = \left\{ CT_{ijk}^{lm} \right\},\ CT_{ijk}^{lm} \in \{1, 2\},\ ijk \in \{I, J, K\} \tag{2}$$

$$V^{lm} = \left\{ V_p^{lm} \right\},\ V_p^{lm} : CT_{ijk}^{lm} = 1,\ ijkp \in \{I, J, K, P\},\ V_{p_1}^{lm} \bigcap V_{p_2}^{lm} = \varnothing,\ p_1 \neq p_2 \tag{3}$$

2.7. Pore Tracking

Each element V_p^{lm} represents a pore in the specimen, for which tracking over time was performed. Since the specimen was removed from the tomograph between scans, the problem of misalignment of its spatial position and orientation arose for different time points. Correct comparison of data required accurate spatial registration of tomograms, ensuring that each voxel corresponded to the same physical volume of material at all stages of the study. Image registration was performed using a method based on identifying stable internal reference points. The centers of mass of the three largest pore cavities identified on each tomogram were used as such reference points. These pores were considered as topologically stable elements of the material structure, allowing changes in the pore space during degradation to be tracked [42].

For pore matching between time steps, nearest-neighbor tracking was used, a method widely applied in 4D tomography of porous media [43–45]. Matching was performed sequentially between consecutive scans, from 28 to 14 days and then from 14 to 0 days. For each pore center of mass, the corresponding pore in the earlier scan was identified as the nearest point by Euclidean distance. This search was performed using a Delaunay triangulation of the earlier scan's pore centers [46]. The triangulation partitions the point set into simplices, so that the enclosing simplex of a query point can be found directly, without an exhaustive comparison against every pore.

For each pore, the center of mass coordinates (4), distance from the specimen center C_{cem}^{lm} to the pore center (5), volume V, and equivalent radius (6) were determined. From the three scans, volumetric strain was calculated for the second and third test stages (7).

$$C^{lm} = \left\{ C_p^{lm} \right\},\ C_p^{lm} \in N \tag{4}$$

$$L_p^{lm} = \| C_{cem}^{lm} - C_p^{lm} \| \tag{5}$$

$$R_p^{lm} = \left(\frac{3V_p^{lm}}{4\pi} \right)^{1/3} \tag{6}$$

$$\varepsilon_{V_p}^{km} = \frac{V_p^{km} - V_p^{0m}}{V_p^{0m}},\ k = \{14,\ 28\}. \tag{7}$$

Analysis of these parameters enables quantitative tracking of changes in the volume of individual pores depending on their location relative to the specimen center and their initial size. This approach makes it possible to assess the spatial heterogeneity of degradation processes. This is important because the specimen surface is in direct contact with the aggressive medium, while the medium penetrates into deeper layers progressively. Furthermore, this approach allows identification of differences in the behavior of pores of different sizes during exposure. The entire CT data analysis algorithm was implemented using the MATLAB R2024a software package.

3. Results

3.1. Mechanical Testing

The compressive strength test results are shown in Figure 4. The mechanically activated specimens exhibited higher initial strength—59.3 MPa compared with 44.5 MPa for the control ones. After 28 days of exposure to the aggressive medium, the strength of the control specimens decreased to 27.6 MPa (a loss of 38%), while that of the mechanically activated specimens dropped to 44.2 MPa (a loss of 25.5%). The slope of a linear fit to the three measured strength values was −0.6 MPa/day for the control specimens and −0.54 MPa/day for the activated specimens. Given the limited number of time points, this slope is presented as a descriptive summary of the trend rather than an established degradation rate. The graph shows similar behavior for both types, differing only in the initial strength level. Error bars in Figure 4 represent the standard deviation across the three specimens, which did not exceed 12% of the mean value at any time point.

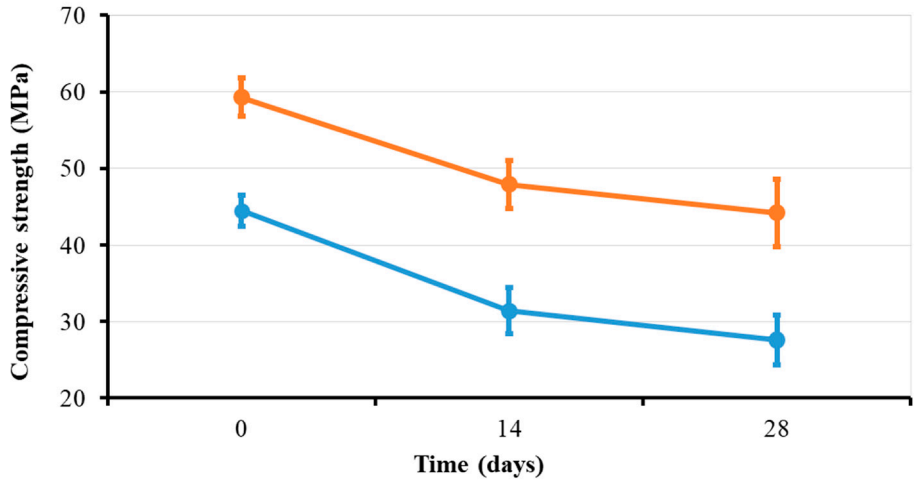


Figure 4. Compressive strength of control (blue) and mechanically activated (orange) specimens during exposure to the model aggressive environment.

3.2. XCT

One marked control specimen and one marked mechanically activated specimen were examined by XCT before exposure and after 14 and 28 days of exposure to the aggressive medium. Figure 5 presents a three-dimensional visualization of the pore space evolution. The mechanically activated specimen shows considerably smaller visual changes in its internal structure compared with the control specimen.

XCT enables the determination of the volumes of different structural fractions of the material by counting the number of voxels belonging to each fraction. Given the voxel size of 32.432 μm, only pores at or above this scale are resolved, so the porosity values reported below represent XCT-resolvable porosity rather than the total porosity of the material. As shown in Figure 6, at 0 days of exposure, the porosity of the control specimen was 1.0% with a total specimen volume of 7662.7 mm^3. The mechanically activated specimens had higher initial porosity—1.5% with a total specimen volume of 7815.4 mm^3. After 14 days, the total specimen volume decreased to 4442.7 mm^3 for the control specimen (a reduction of 42%) and to 6434.8 mm^3 for the activated specimen (a reduction of 18%), while porosity remained close to the initial values for both. After 28 days, the control specimen volume decreased further to 3373.5 mm^3 (a total reduction of 56%), with porosity decreasing slightly to 0.9%. The activated specimen volume decreased to 5718.9 mm^3 (a total reduction of 27%), while porosity remained almost unchanged at 1.5%. Despite its higher initial porosity,

the activated specimen thus exhibited substantially smaller volumetric loss and greater stability of porosity throughout exposure.

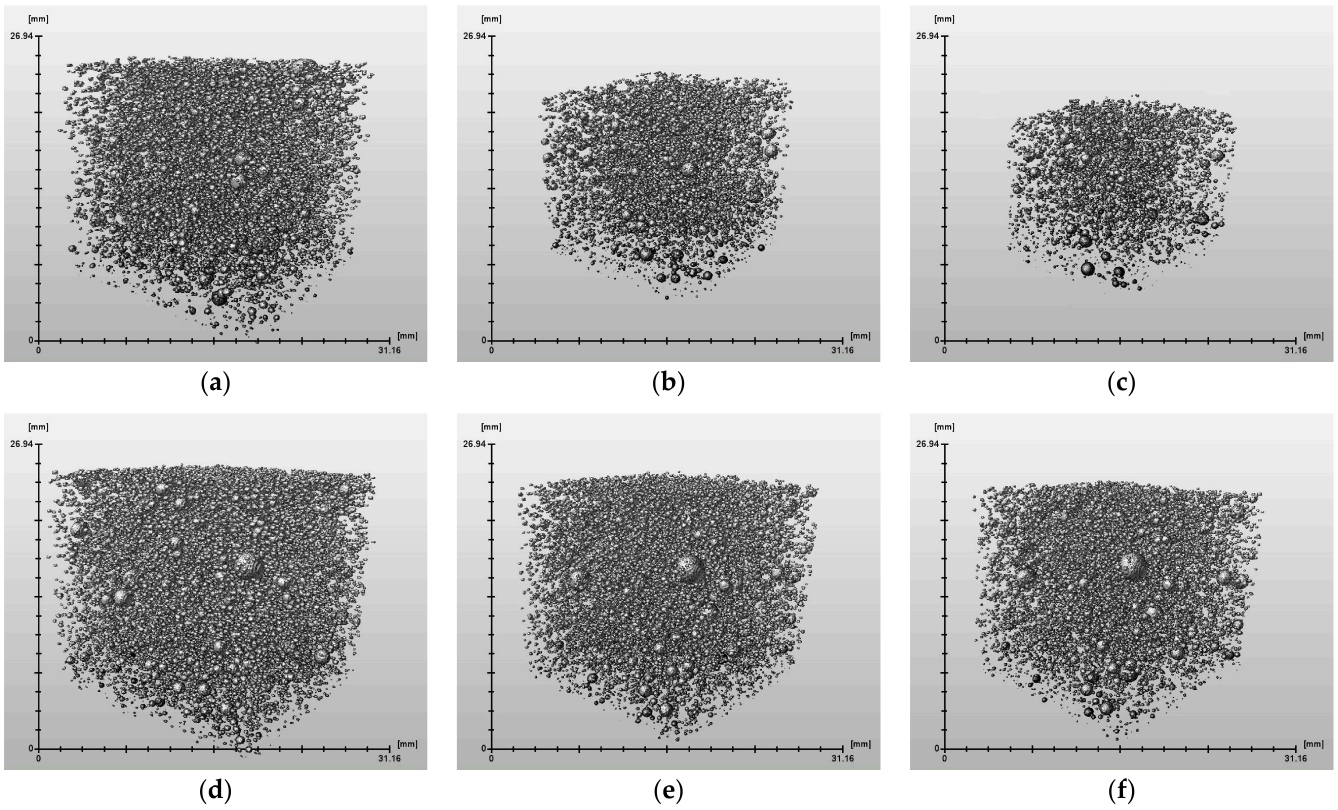


Figure 5. 3D visualization of the pore space: (**a**–**c**) control specimens; (**d**–**f**) mechanically activated specimens; (**a**,**d**) 0 days; (**b**,**e**) 14 days; (**c**,**f**) 28 days.

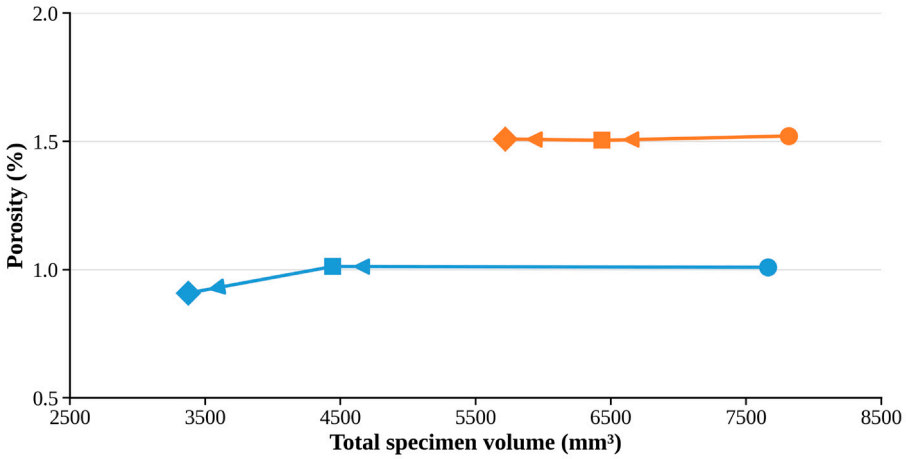


Figure 6. XCT-resolvable porosity versus total specimen volume for control (blue) and mechanically activated (orange) specimens. Different symbols represent different exposure times: circle—day 0, rectangle—day 14, diamond—day 28. Arrows indicate the direction of temporal progression.

In total, tracking was performed for approximately 5600 pores in the control specimen and 10,000 pores in the activated specimen. Consider the violin plots [47] shown in Figure 7, which present the pore radius distribution in two types of cement specimens: control (blue) and mechanically activated in the vortex layer device (orange). Each plot corresponds to one test stage. The vertical axis shows pore radii in millimeters within the range of 0.04 to 0.16 mm. The plots demonstrate the density distribution of pore radius

values, where the width of the violin is proportional to the data density in that region. Extreme outliers, defined as values outside the 5th–95th percentile range, were excluded from the visualization to prevent them from distorting the shape of the distribution. As a result, approximately 5200 pores were shown for the control specimen and 9300 pores for the activated specimen. Inside each plot, boxplots are also shown, reflecting the main statistical characteristics of the distribution: median (line inside the box), mean (asterisk), and quartiles (box boundaries).

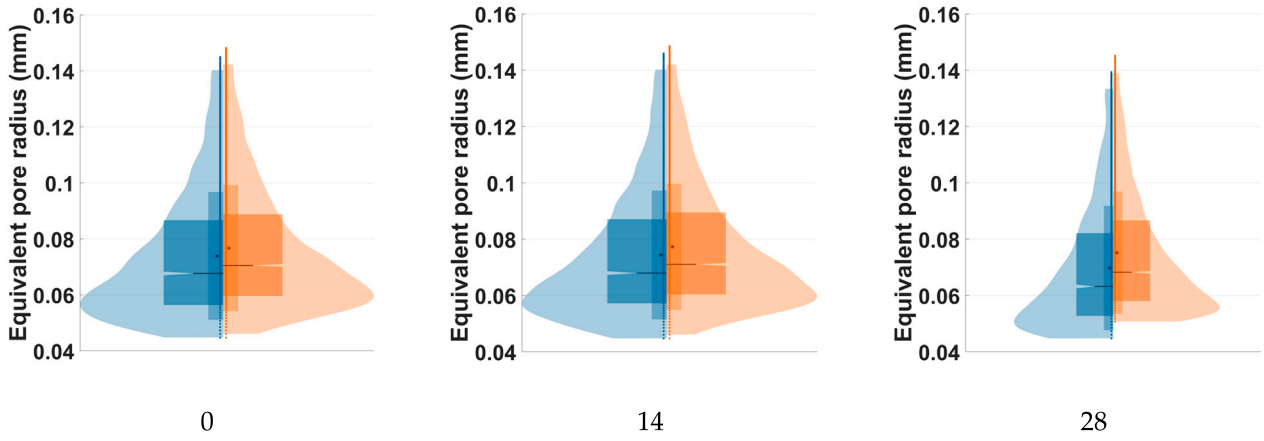


Figure 7. Violin plots of equivalent pore radii for control (blue, $n \approx 5200$) and activated (orange, $n \approx 9300$) specimens.

Analysis of the plots shows that the pore radius distribution in both specimens has a pronounced peak in the range of 0.04–0.08 mm, indicating the dominance of pores of this size and suggesting that the bulk of the pores remain in a similar range. However, in the specimen subjected to activation in the vortex layer device, a shift toward larger radii is observed compared with the control cement at all test stages. Despite a slight shift in the median for the activated specimen, the distributions still largely overlap, suggesting a limited effect of activation on the pore radius distribution. Also, at all stages of the experiment, a similar trend is observed: slight changes in pores at the second step and a noticeable decrease in pore radii toward the third step, indicating a similar character of the processes occurring in the material over time. The dynamics of pore radius changes during the experiment demonstrate that the activated cement undergoes less intense changes compared with the control specimen, indicating a more stable and slowly evolving pore structure. At 28 days, the violins are noticeably narrower in horizontal width than at the earlier stages for both specimens. Because the number of analyzed pores remains nearly unchanged across time points, this narrowing reflects a lower peak density, that is, a more dispersed distribution of pore radii, rather than a difference in sample size.

The spatial–size distribution of individual pores is shown in Figures 8 and 9. In the diagrams, each point corresponds to a single pore: the abscissa shows the distance from the pore center of mass to the specimen center, and the ordinate shows the equivalent pore radius in the initial state. The color indicates the volumetric strain of the pore at 14 (Figure 8) and 28 (Figure 9) days. For better visualization, each figure presents two subplots: (a) for the control specimen and (b) for the activated specimen; the color scale distinguishes pores that increased in volume from those that decreased. Pores with an equivalent radius below 0.05 mm were excluded due to the difficulty of spatial detection over time. Points with a relative volume change of less than 0.05 are also not displayed. This allows tracking of the sizes and positions of only those pores that undergo noticeable volume changes.

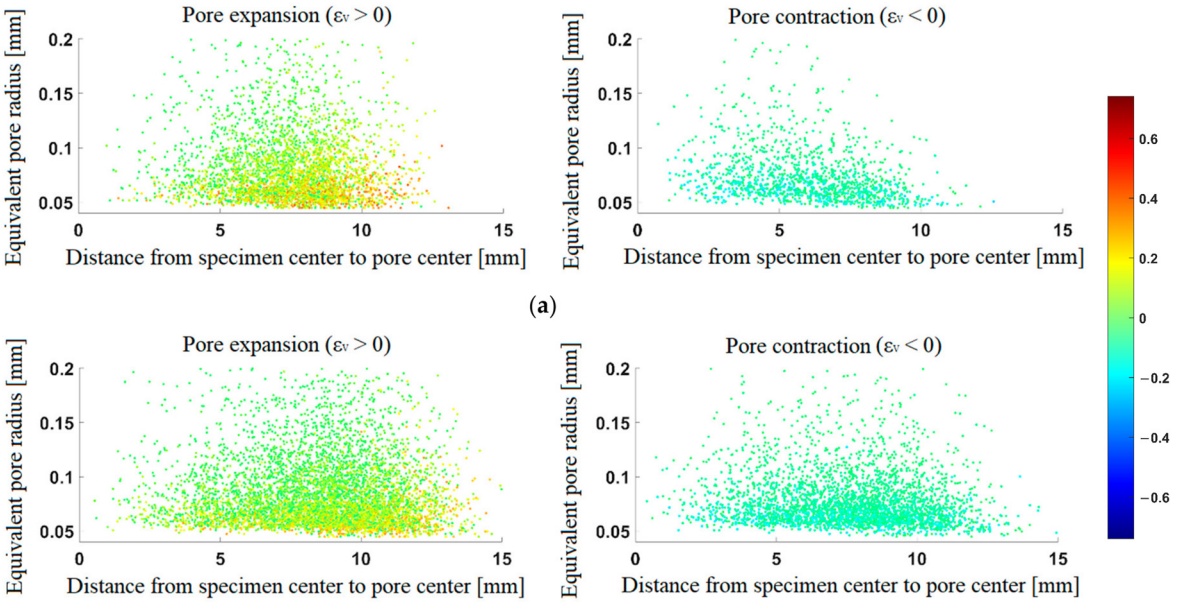


Figure 8. Pore distribution by distance from the specimen center and equivalent radius, with indication of volumetric strain after 14 days for the control (**a**) and activated (**b**) specimens.

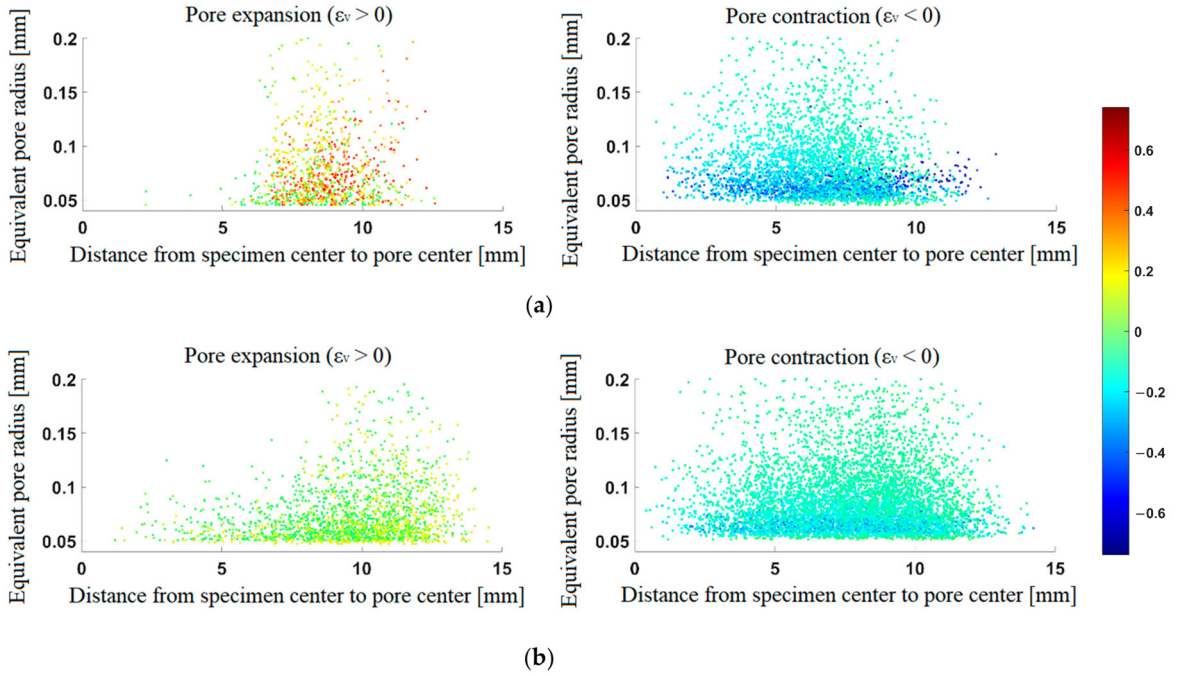


Figure 9. Pore distribution by distance from the specimen center and equivalent radius, with indication of volumetric strain after 28 days for the control (**a**) and activated (**b**) specimens.

Analysis of the diagrams shows that the most intense changes in pore volume—especially their expansion—occur in the near-surface layers of the specimens. Pore infilling (volume decrease) is more pronounced for small pores, as seen by the band of blue points limited to a radius of 0.05–0.1 mm. All the described degradation processes of the pore space proceed qualitatively similarly for both control and activated specimens, but are quantitatively noticeably more active in the control specimen. The XCT data indicate the higher structural stability of the mechanically activated specimen to the acid environment, despite its higher initial porosity.

4. Discussion

The results obtained in this study show that the mechanically activated specimens, which also had a higher specific surface area, exhibited better resistance to acid media than the control specimens. Moreover, the use of XCT allowed a deeper insight into the mechanisms of this degradation than traditional methods provide.

4.1. Degradation Kinetics and Mechanical Properties

The observed rates of strength loss (0.6 MPa/day for the control and 0.54 MPa/day for the modified samples) are very similar, given the limited number of data points. This indicates that mechanical activation does not alter the chemical mechanism of matrix degradation but instead provides the material with a higher initial strength reserve (59.3 MPa vs. 44.5 MPa). A similar conclusion was reached in the study [18], which demonstrated similar mass-change kinetics for the same compositions but lacked data on the spatial structure of the degradation process. Our results suggest that the activated and control specimens follow a similar pattern of strength loss over time, but the activated specimens start from a higher initial strength and retain a greater share of it, which helps preserve the structural integrity of the matrix.

4.2. Evolution of Pore Space

It was previously hypothesized that secondary reaction products precipitate and clog the pores of the cement matrix [15,16,18]. Our data confirm that porosity, as an integral parameter, is uninformative: in control samples, it remained virtually unchanged (shifting from 1.0% to 0.9%), whereas the volume decreased by 56%. This is explained by the superposition of leaching (which removes both the matrix and pores) and the filling of pores with secondary products. Consequently, a change in total sample volume is a more reliable criterion for assessing durability than porosity. Activated samples lost only 27% of their volume despite having a higher initial porosity (1.5%), indicating that the structural framework remained intact.

These results align with studies showing a lack of direct correlation between porosity and durability. In [14], the incorporation of microcapsules into geopolymers reduced gas permeability despite an increase in total porosity; in [48], the gas permeability of alkali-activated concretes varied thirtyfold with a porosity change of only 3 percentage points; and in [49], total porosity decreased following geopolymer leaching, yet the pore size distribution shifted toward larger pores. This confirms that pore architecture and connectivity—rather than volume—play the decisive role. It can be hypothesized that mechanical activation creates a more homogeneous and less interconnected pore system; however, as direct measurements of connectivity or gas permeability were not performed in this study, this remains merely a hypothesis. Tracking individual pores (Figures 8 and 9) made it possible to quantitatively assess the spatial heterogeneity of degradation for the first time. It was found that pore expansion is localized in the near-surface layers—a logical outcome given the maximum concentration of aggressive agents at the interface. Pore filling is most pronounced in the 0.05–0.1 mm range; this is likely where secondary salts crystallize, though their localization within the pores was not investigated in earlier studies [15,16,18], so this explanation remains preliminary and requires local chemical analysis (e.g., XCT with EDS). Qualitatively, the degradation pattern is identical for control and activated samples; quantitatively, however, the activated samples exhibit less pronounced pore expansion in the near-surface zone and less filling of small pores, consistent with lower volumetric loss (27% vs. 56%) and stable porosity (1.5%). Thus, the pore-level degradation process appears qualitatively similar in both specimens, but it is quantitatively less pronounced in the activated specimen, preserving the structural integrity of the matrix.

4.3. Practical Significance and Directions for Future Research

The results highlight the promise of using mechanically activated cements for construction of structures exposed to biogenic acid attack: wastewater treatment plants, sewer systems, and floors in the food and chemical industries. However, the data presented do not allow these findings to be directly extrapolated to concrete structures. The present study was conducted on hardened cement paste (HCP) without coarse aggregate. The presence of coarse aggregate in real concrete may affect the migration pathways of the aggressive medium and form an interfacial transition zone (cement paste–aggregate), as shown in [50]. A second limitation is that the model medium used here reproduces the chemical products of microbial metabolism but not the biological process itself (e.g., biofilm formation and continuous in-situ acid generation), so the performance of activated cement under direct microbial colonization remains to be established. However, this requires conducting research in specialized microbiological laboratories. Moreover, the mass change study in our previous work [18] showed that active processes—the transition from mass increase to mass loss—occur during the period up to 14 days, which would also be worth investigating with higher temporal frequency in the tomograph.

5. Limitations

This study has several limitations that should be considered when interpreting the results.

1. The experiments were performed on hardened cement paste rather than on mortar or concrete. Validation under conditions closer to real structures, including the presence of aggregate, is still required.
2. The model medium reproduces only the chemical component of microbial metabolism. It does not include biofilm formation or continuous in-situ acid generation, so material behavior under direct microbial colonization remains to be established.
3. Compressive testing was performed on three specimens per group, which limits the statistical reliability of the reported strength values.
4. The specimen size (20 × 20 × 20 mm) is smaller than that specified by standard compressive strength test methods. This size was required by the field-of-view and resolution constraints of XCT scanning and may have influenced the measured mechanical response.
5. XCT scanning and pore tracking were performed on a single specimen per group, without replication. The observed porosity and volumetric changes should therefore be regarded as representative rather than statistically validated.
6. Pore tracking assumed a one-to-one correspondence between pores in consecutive scans, without separately identifying pore appearance, disappearance, splitting, or merging. This may introduce some uncertainty into individual pore trajectories, although it does not affect the specimen-scale volume and porosity results.
7. The study did not include a reference cement of comparable fineness obtained by conventional grinding. Therefore, the observed improvement cannot be unambiguously attributed to the specific effects of mechanical activation in a vortex layer device rather than to the general effect of increased specific surface area. Future work should include such a reference to separate these factors.

6. Conclusions

In this study, the effect of a model acid medium on HCP based on control and mechanically activated Portland cement was experimentally evaluated. To assess the evolution of pore space under acid corrosion conditions, XCT with individual pore tracking over time was applied.

Based on the obtained results, the following conclusions can be drawn: the mechanically activated specimens showed better corrosion resistance than the control specimens. Specimens based on activated HCP retained significantly higher compressive strength (44.2 MPa vs. 27.6 MPa for control specimens). A paradox regarding porosity and volumetric stability was observed. Mechanically activated specimens have higher initial porosity (1.5% vs. 1%), yet they demonstrate much greater stability. While control specimens lost 56% of their initial volume, the activated specimens lost only 27%, and their pore structure remained stable. Spatial heterogeneity of degradation was observed in the examined specimens. XCT showed that the most intense pore expansion occurs in the near-surface layers, while pore infilling is characteristic of small pores with radii of 0.05–0.1 mm, which is likely associated with the formation of secondary reaction products.

Traditional methods (mass, strength) provide only an integral assessment of degradation. XCT enables the identification of hidden spatiotemporal patterns of failure, showing that the activated HCP structure was more resistant to leaching even with a larger initial pore volume.

The obtained data justify further research into the use of Portland cement mechanically activated in a vortex layer device for applications exposed to biogenic acid attack. However, validation on mortar and concrete under conditions closer to real structures is required.

Author Contributions: Conceptualization, R.I. and O.S.; methodology, R.I., O.S. and F.S.; software, E.S. and O.G.; validation, O.G., T.B. and B.T.; formal analysis, E.S. and F.S.; investigation, R.I., R.K. and T.B.; resources, R.I. and R.K.; data curation, R.I. and R.K.; writing—original draft preparation, F.S. and E.S.; writing—review and editing, F.S. and O.S.; visualization, B.T. and O.S.; supervision, F.S. and O.S.; funding acquisition, O.S. All authors have read and agreed to the published version of the manuscript.

Funding: This research was funded by the subsidy allocated to Kazan Federal University for the state assignment in the sphere of scientific activities, project No. FZSM-2026-0006.

Data Availability Statement: The original contributions presented in this study are included in the article. Further inquiries can be directed to the corresponding author.

Conflicts of Interest: The authors declare no conflicts of interest.

Abbreviations

The following abbreviations are used in this manuscript:

XCT	X-ray computed tomography
HCP	Hardened cement paste

References

1. Muhit, I.B.; Al-Fakih, A.; Suntharalingam, T.; Michel, A. Progress in Computational Modelling for Concrete Durability and Its Integration with Artificial Intelligence and Life-Cycle Assessment. *Arch. Comput. Methods Eng.* **2026**, *33*, 2751–2783. [CrossRef]
2. Ma, J.; Yang, Q.; Peng, X.; Xia, K. Review on Durability Deterioration and Mitigation of Concrete Structures. *Coatings* **2025**, *15*, 982. [CrossRef]
3. Bertron, A. Understanding interactions between cementitious materials and microorganisms: A key to sustainable and safe concrete structures in various contexts. *Mater. Struct.* **2014**, *47*, 1787–1806. [CrossRef]
4. Povedano-Priego, C.; Jroundi, F. Microbial Processes in Concrete as Anthropogenic Biogeochemical Ecosystems: Biodeterioration Mechanisms and Biotechnological Strategies. *Rev. Environ. Sci. Biotechnol.* **2026**, *25*, 30. [CrossRef]
5. Wang, D.; Guan, F.; Feng, C.; Mathivanan, K.; Zhang, R.; Sand, W. Review on Microbially Influenced Concrete Corrosion. *Microorganisms* **2023**, *11*, 2076. [CrossRef]
6. Yang, H.; Jiang, L.; Zhang, Y.; Pu, Q.; Xu, Y. Predicting the Calcium Leaching Behavior of Cement Pastes in Aggressive Environments. *Constr. Build. Mater.* **2012**, *29*, 88–96. [CrossRef]

7. Omrane, M.; Mouli, M.; Benosman, A.; Senhadji, Y. Deterioration of Mortar Composites in Acidic Environment. *Adv. Mater. Res.* **2014**, *1064*, 3–8. [CrossRef]
8. Gîrboveanu, A.; Jebli, M.; Jamin, F.; Huon, V.; Bonnet, L.; Georgescu, D.; El Youssoufi, M.S. Mechanical Tensile Behaviour of Cement Paste/Aggregate Bond Exposed to Leaching. *Constr. Build. Mater.* **2023**, *369*, 130592. [CrossRef]
9. Babaahmadi, A.; Tang, L.; Abbas, Z.; Martensson, P. Physical and Mechanical Properties of Cementitious Specimens Exposed to an Electrochemically Derived Accelerated Leaching of Calcium. *Int. J. Concr. Struct. Mater.* **2015**, *9*, 295–306. [CrossRef]
10. Esaker, M.; Hamza, O.; Souid, A.; Elliott, D. Self-Healing of Bio-Cementitious Mortar Incubated within Neutral and Acidic Soil. *Mater. Struct.* **2021**, *54*, 96. [CrossRef]
11. Koenig, A.; Dehn, F. Biogenic Acid Attack on Concretes in Biogas Plants. *Biosyst. Eng.* **2016**, *147*, 226–237. [CrossRef]
12. Beddoe, R.E.; Dorner, H.W. Modelling Acid Attack on Concrete: Part I. The Essential Mechanisms. *Cem. Concr. Res.* **2005**, *35*, 2333–2339. [CrossRef]
13. Damion, T.; Cepuritis, R.; Chaunsali, P. Sulfuric Acid and Citric Acid Attack of Calcium Sulfoaluminate-Based Binders. *Cem. Concr. Compos.* **2022**, *130*, 104524. [CrossRef]
14. El Moustapha, B.; Bonnet, S.; Khelidj, A.; Leklou, N.; Maranzana, N.; Ahmedou Babah, I. Influence of microencapsulated phase change materials on drying shrinkage, pore structure, and gas permeability of blast-furnace slag and metakaolin-based geopolymers. *J. Sustain. Cem.-Based Mater.* **2025**, *14*, 2424–2440. [CrossRef]
15. Ibragimov, R.A.; Korolev, E.V.; Deberdeev, T.R.; Leksin, V.V. Efficient Complex Activation of Portland Cement through Processing It in the Vortex Layer Machine. *Struct. Concr.* **2019**, *20*, 851–859. [CrossRef]
16. Ibragimov, R.; Korolev, E.; Potapova, L.; Deberdeev, T.; Khasanov, A. The Influence of Physical Activation of Portland Cement in the Electromagnetic Vortex Layer on the Structure Formation of Cement Stone: The Effect of Extended Storage Period and Carbon Nanotubes Modification. *Buildings* **2022**, *12*, 711. [CrossRef]
17. Stel'makh, S.; Mailyan, L.; Beskopylny, A.; Shcherban', E.; Shuiskii, A. Influence of Technological Factors of Cement Mechanical Activation on the Strength Properties of Fine-Grained Concrete. In *Networked Control Systems for Connected and Automated Vehicles*; Guda, A., Ed.; Lecture Notes in Networks and Systems; Springer: Cham, Switzerland, 2023; Volume 510, pp. 1671–1680. [CrossRef]
18. Ibragimov, R.; Shakirzyanov, F.; Kayumov, R.; Korolev, E. The Influence of the Aggressive Medium upon the Degradation of Concrete Structures: Numerical Model of Research. *Buildings* **2024**, *14*, 1762. [CrossRef]
19. Guessoum, M.; El Moustapha, B.; Khadraoui, F.; Chateigner, D.; Gascoin, S.; Maherzi, W. Effect of Scallop Shell Powder Addition on Fresh and Hardened Properties of Self-Compacting Concrete (SCC) Based on Recycled Aggregates. *Constr. Build. Mater.* **2025**, *495*, 143660. [CrossRef]
20. Gerasimov, O.; Koroleva, E.; Sachenkov, O. Experimental Study of Evaluation of Mechanical Parameters of Heterogeneous Porous Structure. *IOP Conf. Ser. Mater. Sci. Eng.* **2017**, *208*, 012013. [CrossRef]
21. Gerasimov, O.; Kharin, N.; Vorob'yev, O.; Semenova, E.; Sachenkov, O. Determination of the Mechanical Properties Distribution of the Sample by Tomography Data. *J. Phys. Conf. Ser.* **2019**, *1158*, 022046. [CrossRef]
22. Kharin, N.; Akifyev, K.; Spiridonova, K.; Statsenko, E.; Semenova, E.; Bolshakov, P.; Sachenkov, O. Inter-Track Porosity and Macroporosity Insights into Mechanical Properties of FDM Printed Samples Using In-Situ 4D XCT. *Int. J. Mech. Mater. Des.* **2025**, *21*, 1239–1257. [CrossRef]
23. Brisard, S.; Serdar, M.; Monteiro, P.J.M. Multiscale X-Ray Tomography of Cementitious Materials: A Review. *Cem. Concr. Res.* **2020**, *128*, 105824. [CrossRef]
24. Taheri-Shakib, J.; Al-Mayah, A. 4D Evolutions of Cracks, Voids, and Corrosion Products in Reinforced Concrete Materials. *Sci. Rep.* **2023**, *13*, 22455. [CrossRef]
25. Du Plessis, A.; Boshoff, W.P. A Review of X-Ray Computed Tomography of Concrete and Asphalt Construction Materials. *Constr. Build. Mater.* **2019**, *199*, 637–651. [CrossRef]
26. Ramaswamy, K.P.; Santhanam, M. A Study of Deterioration of Cement Paste Due to Acid Attack Using X-Ray Computed Micro-Tomography. *Adv. Cem. Res.* **2018**, *30*, 123–138. [CrossRef]
27. Su, Z.; Yue, Z.; Paul, P.P.; Liu, X.; Marsh, A.T.M.; Unluer, C.; Provis, J.L.; Burnett, T.L.; Bernal, S.A.; Withers, P.J. 4D Imaging of Microstructural Evolution in Alkali-Activated Slag Cement Pastes: Linking Pore-Network Topology to Performance. *Cem. Concr. Compos.* **2026**, *166*, 106382. [CrossRef]
28. Guan, Z.; Fan, H.; Zhang, Y.; Sun, G.; Wang, Y.; Zhang, Y. Mesoscopic Damage Evolution and Numerical Simulation of Cement Paste after High-Temperature Exposure Based on Quasi In Situ 4D X-Ray CT Technology. *J. Build. Eng.* **2026**, *132*, 117328. [CrossRef]
29. Stroganov, V.; Sagadeev, E.; Ibragimov, R.; Potapova, L. Mechanical Activation Effect on the Biostability of Modified Cement Compositions. *Constr. Build. Mater.* **2020**, *246*, 118506. [CrossRef]
30. De Graef, B.; Cnudde, V.; Dick, J.; De Belie, N.; Jacobs, P.; Verstraete, W. A Sensitivity Study for the Visualisation of Bacterial Weathering of Concrete and Stone with Computerised X-Ray Microtomography. *Sci. Total Environ.* **2005**, *341*, 173–183. [CrossRef]

31. *EN 197-1:2011*; Cement—Part 1: Composition, Specifications and Conformity Criteria for Common Cements. CEN: Brussels, Belgium, 2011.
32. *EN 196-3:2016*; Methods of Testing Cement—Part 3: Determination of Setting Times and Soundness. CEN: Brussels, Belgium, 2016.
33. *ASTM C109/C109M-20*; Standard Test Method for Compressive Strength of Hydraulic Cement Mortars (Using 2-in. or [50-mm] Cube Specimens). ASTM International: West Conshohocken, PA, USA, 2020.
34. *EN 196-1:2016*; Methods of Testing Cement—Part 1: Determination of Strength. CEN: Brussels, Belgium, 2016.
35. *ISO 679:2009*; Cement—Test Methods—Determination of Strength. ISO: Geneva, Switzerland, 2009.
36. Yakovleva, G.; Sagadeev, E.; Stroganov, V.; Kozlova, O.; Okunev, R.; Ilinskaya, O. Metabolic Activity of Micromycetes Affecting Urban Concrete Constructions. *Sci. World J.* **2018**, *2018*, 8360287. [CrossRef]
37. Ibragimov, R.A.; Shakirzyanov, F.R.; Kayumov, R.A.; Korolev, E.V. Evaluation of the Influence of an Aggressive Environment on the Durability of the Cement Stone. *Constr. Mater. Prod.* **2024**, *7*, 4. [CrossRef]
38. Strokin, K.; Novikov, D.; Konovalova, V. Forecasting the Durability of Reinforced Concrete under Conditions of Microbiological Corrosion. *E3S Web Conf.* **2021**, *274*, 04003. [CrossRef]
39. *EN 12390-3:2019*; Testing Hardened Concrete—Part 3: Compressive Strength of Test Specimens. CEN: Brussels, Belgium, 2019.
40. Otsu, N. A Threshold Selection Method from Gray-Level Histograms. *IEEE Trans. Syst. Man. Cybern.* **1979**, *9*, 62–66. [CrossRef]
41. Thakur, M.M.; Enright, S.; Hurley, R.C. Phase Segmentation in X-Ray CT Images of Concrete with Implications for Mesoscale Modeling. *Constr. Build. Mater.* **2023**, *403*, 133033. [CrossRef]
42. Withers, P.J.; Bouman, C.; Carmignato, S.; Cnudde, V.; Grimaldi, D.; Hagen, C.K.; Maire, E.; Manley, M.; Du Plessis, A.; Stock, S.R. X-Ray Computed Tomography. *Nat. Rev. Methods Primers* **2021**, *1*, 18. [CrossRef]
43. Andò, E.; Viggiani, G.; Hall, S.A.; Desrues, J. Experimental Micro-Mechanics of Granular Media Studied by X-Ray Tomography: Recent Results and Challenges. *Geotech. Lett.* **2013**, *3*, 142–146. [CrossRef]
44. Maire, E.; Withers, P.J. Quantitative X-Ray Tomography. *Int. Mater. Rev.* **2014**, *59*, 1–43. [CrossRef]
45. Akifyev, K.; Kharin, N.; Spiridonova, K.; Statsenko, E.; Semenova, E.; Bolshakov, P.; Sachenkov, O. Research of Inter-Track and Macroporosity, and Fluid Content in Determining Mechanical Performance of 3D-Printed Unit Cells: Insights From In Situ 4D X-Ray Tomography. *Adv. Eng. Mater.* **2026**, *28*, e202500396. [CrossRef]
46. Barber, C.B.; Dobkin, D.P.; Huhdanpaa, H. The Quickhull Algorithm for Convex Hulls. *ACM Trans. Math. Softw.* **1996**, *22*, 469–483. [CrossRef]
47. Hintze, J.L.; Nelson, R.D. Violin Plots: A Box Plot-Density Trace Synergism. *Am. Stat.* **1998**, *52*, 181–184. [CrossRef]
48. Duży, P.; Colombel, M.C.; Hager, I.; Amiri, O. The Effect of Preconditioning Temperature on Gas Permeability of Alkali-Activated Concretes. *Materials* **2023**, *16*, 4143. [CrossRef]
49. Nguyen, T.N.; Phung, Q.T.; Jacques, D.; Elsen, J.; Pontikes, Y. Microstructure and Transport Properties of Metakaolin-Based Geopolymers Subjected to Accelerated Leaching. *Constr. Build. Mater.* **2024**, *426*, 136225. [CrossRef]
50. Xia, L.; Jiang, C.; Chen, G.; Li, S. Multiscale Damage Evolution in Hydraulic Concrete under Cyclic Freeze–Thaw and Calcium Leaching: From Microstructural Degradation to Macroscopic Performance. *Constr. Build. Mater.* **2025**, *494*, 143481. [CrossRef]

Disclaimer/Publisher's Note: The statements, opinions and data contained in all publications are solely those of the individual author(s) and contributor(s) and not of MDPI and/or the editor(s). MDPI and/or the editor(s) disclaim responsibility for any injury to people or property resulting from any ideas, methods, instructions or products referred to in the content.